

11 ABSTRACT: We develop a novel single-column model of clear-sky radiative-advective equilib-
12 rium where advective heating is internally determined by relaxing the column temperature and
13 humidity toward fixed midlatitude profiles, consistent with an air-mass transformation perspective.
14 The model reproduces observed polar temperature and advective heating rate profiles, and also
15 captures many of the climate-change responses found in climate models. Exploring the model's
16 physics, we show that the surface-based temperature inversion develops by ceding energy down-
17 wards to the surface, which then radiates this energy to space; we name this the "surface radiator fin"
18 effect. We use the model to address three outstanding questions regarding polar climate change: (i)
19 What mechanisms control polar lapse-rate change? (ii) What determines the known compensation
20 between changes in dry and moist energy transport? and (iii) What is the most physically consistent
21 way to decompose forcing and feedbacks at the poles? Within the model, the answers to these
22 questions are: (i) Three mechanisms control the lapse-rate response to warming: weakening of
23 the surface radiator fin, increased radiative cooling by free-tropospheric water vapor emission, and
24 relaxation toward the external profile anomaly; all three increase the lapse rate as climate warms.
25 (ii) Compensation between dry and moist advective heating results from a delicate balance be-
26 tween changes in the boundary layer and the free troposphere, with no constraints imposing precise
27 compensation. (iii) Remote advective influence on the poles should be considered a forcing, while
28 lapse-rate and advective heating changes jointly contribute to the temperature feedback.

29 **1. Introduction**

30 The concept of radiative-convective equilibrium (RCE) and its embodiment in a single-column
31 model (Manabe and Strickler 1964; Manabe and Wetherald 1967) is the foundation of our un-
32 derstanding and quantification of climate sensitivity (see review by Jeevanjee et al. 2022). RCE
33 prevails when the atmosphere is heated from below and atmospheric radiative cooling to space is
34 balanced by upward turbulent fluxes at the surface. In RCE, surface and atmospheric temperature
35 are strongly coupled while atmospheric temperature is constrained to follow a moist adiabatic
36 profile, imposing a tight connection between surface temperature and top-of-atmosphere (TOA)
37 energy fluxes. As a result, a unit perturbation of TOA flux will give the same surface temperature
38 response regardless of which forcing or feedback agent provides the perturbation. This fungibility
39 motivates the now-conventional TOA forcing-feedback decomposition (Manabe and Wetherald
40 1980; Sherwood et al. 2015). This decomposition includes a separate lapse-rate feedback, which is
41 reasonable since in RCE the lapse-rate feedback is constrained by the moist adiabat and constitutes
42 a distinct physical mechanism.

43 The opposite limit to RCE is radiative-advective equilibrium (RAE), where diabatic cooling is
44 primarily balanced by lateral energy flux convergence (Payne et al. 2015; Cronin and Jansen 2016).
45 RAE prevails in the polar regions, especially in winter (Miyawaki et al. 2022, 2023), affecting
46 regional and global-mean radiative feedbacks (Feldl and Merlis 2023). RAE is crucial to polar
47 amplification—the enhanced warming of the poles in response to global forcing that is a robust
48 but still not fully understood feature of Earth’s climate sensitivity (Previdi et al. 2021; Taylor et al.
49 2022). This motivates interest in developing a minimal model of RAE that robustly captures the
50 basic physics of high-latitude climate, as a counterpart to single-column RCE for lower latitudes.

51 Substantial progress has been made in this direction (Payne et al. 2015; Cronin and Jansen 2016;
52 Henry and Merlis 2020; Henry et al. 2021; Freese and Cronin 2021). This previous work shows
53 that RAE is profoundly different from RCE. In RAE, fungibility is lost: the surface response to
54 unit TOA forcing depends on the nature of the forcing. Also, different forcings affect the lapse rate
55 differently; for example, changes in greenhouse gases and in surface solar absorption both give
56 a bottom-amplified response, while changes in advective heating tend to stabilize the atmosphere
57 (Lu and Cai 2010; Cronin and Jansen 2016; Henry et al. 2021). This means that it no longer makes
58 sense to think of lapse-rate feedback as a single, standalone mechanism but rather as the residual

59 of disparate effects (Lu and Cai 2009; Cai and Lu 2009). It also raises basic questions, such as why
60 a well-mixed gas like CO₂ should give a similar lapse-rate response to a surface forcing, and why
61 both of these are different from the response to advective heating. These are important questions
62 considering the major role attributed to lapse-rate feedback in explaining polar amplification by
63 the conventional TOA decomposition (Pithan and Mauritsen 2014; Hahn et al. 2021).

64 The central difficulty in formulating a single-column RAE model is how to specify advective
65 heating. Advection depends on horizontal gradients which are not represented in a single-column
66 model. In prior work this problem is circumvented by prescribing a fixed profile of advective
67 heating. But in RAE, advective heating must balance diabatic cooling. A change to radiative
68 cooling within the column—due for example to changing greenhouse gas concentrations—will
69 automatically result in changed advective heating. Keeping advective heating fixed breaks this
70 connection. Advective heating should be internally determined as part of the solution, but this
71 requires information about extra-polar fields not available in a single polar column.

72 A potential way forward is suggested by the results of climate model simulations where radiative
73 forcing is applied within limited latitude bands (Chung and Räisänen 2011; Yoshimori et al. 2017;
74 Shaw and Tan 2018; Stuecker et al. 2018; Semmler et al. 2020). These simulations all show that
75 while the poles respond strongly to forcing applied in lower latitudes, the opposite is not true:
76 midlatitude temperatures are to a first approximation unaffected by polar forcing. This suggests
77 that conditions at the poleward edge of the midlatitudes provide a boundary condition for the
78 polar climate. By appropriately including this boundary condition in a single-column model, it
79 would be possible to simulate changes internal to the polar column while keeping this boundary
80 condition fixed, or simulate remote effects on the poles by changing the boundary condition, all
81 while allowing advective heating to adjust in a physically consistent way.

82 Here, our first aim is to search for a simple yet sufficiently realistic way to apply the boundary
83 condition. In Section 2, we show that advective heating can be approximated as a simple relaxation
84 toward specified temperature and humidity profiles representative of midlatitude conditions. We
85 implement it in a single-column model using realistic radiation, a simple turbulence scheme and
86 assuming clear-sky conditions. Testing this model against reanalysis shows satisfactory results.

87 Our second aim is to explore the single-column model to better understand the nature of the
88 RAE regime and its response to local and remote perturbations (Sections 3–7). We address the
89 following specific questions:

- 90 1. What mechanisms control the polar lapse-rate response to global warming? Specifically, why
91 is there a climatological surface-based temperature inversion, and what controls its strength?
- 92 2. Why do changes in moist and dry energy transport to the poles tend to compensate each other
93 (Hwang et al. 2011)—are there any strong constraints acting to enforce this compensation?
- 94 3. What is the best way to decompose forcing and feedbacks at the poles?

95 The relaxation approach used in the single-column model developed here connects directly with
96 the air-mass transformation perspective on polar climate (Pithan et al. 2018). In this perspective,
97 midlatitude maritime air masses are advected into the polar cap, cool diabatically, and exit as
98 polar air masses with lower temperature and humidity. The polar cap is continuously ventilated by
99 an ensemble of such transient air-mass transformation events, and the steady-state single column
100 model aims to capture the average effect of an ensemble of such events. We will emphasize
101 this perspective throughout the paper, as it proves useful in gaining intuitive understanding of the
102 model’s behavior.

103 **2. The single-column model**

104 *a. A simple expression for polar advective heating*

105 We write the temperature tendency $\partial_t T$ at a given point in the polar atmosphere as

$$\partial_t T = Q_{\text{rad}} + Q_{\text{dif}} + Q_{\text{dry}} + Q_{\text{lat}} \quad (1)$$

106 where Q_{rad} and Q_{dif} are heating rates due radiation and vertical turbulent diffusion respectively,
107 Q_{dry} is the advective heating rate due to dry static energy convergence by the large-scale flow, and
108 Q_{lat} is the heating rate due to the latent heat release that accompanies net condensation. In steady
109 state, the net condensation rate equals the rate of moisture convergence. In this case, we can write

$$Q_{\text{adv}} \equiv Q_{\text{dry}} + Q_{\text{lat}} = -\frac{1}{c_p} \nabla \cdot (\mathbf{u}h) \quad (2)$$

110 where $\mathbf{u} = (u, v, \omega)$ is the three-dimensional large-scale wind and $h = c_p T + \ell_v q + gz$ is the moist
 111 static energy (MSE), with c_p the specific heat of air, ℓ_v the latent heat of condensation, q the
 112 specific humidity and gz the geopotential, and we have defined Q_{adv} as the total advective heating
 113 rate. Averaging (2) horizontally over a polar cap (i.e. the region poleward of a given latitude line)
 114 and using the divergence theorem yields

$$c_p \overline{Q_{\text{adv}}} = \frac{1}{L} [vh] - \partial_p \overline{\omega h} \quad (3)$$

115 where $\overline{(\cdot)}$ indicates an area average over the cap, $[\cdot]$ indicates a zonal average around the edge of
 116 the cap, and $L = C/A$ with C the circumference and A the area of the cap. Separating mean and
 117 eddy components, (3) can be rewritten as

$$c_p \overline{Q_{\text{adv}}} = \underbrace{\frac{1}{L} [v] \left([h] - \overline{h} \right)}_{\text{MMC}} - \underbrace{\overline{\omega} \partial_p \overline{h}} + \underbrace{\frac{1}{L} [v^* h^*]}_{\text{Horizontal eddy}} - \underbrace{\partial_p \overline{\omega' h'}}_{\text{Vertical eddy}} \quad (4)$$

118 where stars and primes indicate deviations from the zonal and polar-cap mean respectively. The
 119 first two terms on the r.h.s. represent MSE convergence by the mean meridional circulation (MMC),
 120 the third term represents horizontal MSE convergence by eddies around the edge of the polar cap,
 121 and the last term represents vertical MSE redistribution by eddies within the polar cap.

122 The horizontal eddy term can further be rewritten in terms of inward- and outward-oriented
 123 fluxes defined as

$$v^{\text{in}} = [H(v^*) v^*], \quad h^{\text{in}} = \frac{1}{v^{\text{in}}} [H(v^*) v^* h], \quad h^{\text{out}} = \frac{1}{-v^{\text{in}}} [H(-v^*) v^* h], \quad (5)$$

124 where H is the Heaviside function and we have used $[v^* h^*] = [v^* h]$. In the Northern Hemisphere,
 125 v^{in} is the eddy mass flux flowing *into* the polar cap, while h^{in} and h^{out} are the mass-flux-weighted
 126 mean MSE values of air flowing into and out of the cap respectively. With these definitions, the
 127 horizontal eddy term becomes

$$\frac{1}{L} [v^* h^*] = -\frac{1}{\tau} \left(h^{\text{out}} - h^{\text{in}} \right) \quad (6)$$

128 where

$$\frac{1}{\tau} = \frac{v^{\text{in}}}{L}. \quad (7)$$

129 To understand the relative importance of the various terms in (4), we evaluate them directly using
130 the ERA-Interim reanalysis product. We use 6-hourly data on pressure levels. Horizontal averages
131 exclude ‘underground’ regions where pressure is greater than surface pressure. Following previous
132 work (Overland and Turet 1994; Cardinale et al. 2021), the vertical mean is removed from $[v]$ to
133 exclude spurious contributions from net mass convergence. Results at 65°N (Figure 1c) show that
134 the MMC term in (4) is much smaller than the horizontal eddy term at all levels. Similar results
135 are obtained for other latitudes of the equatorward edge of the polar cap between 60-80°N (not
136 shown).

137 Separating the horizontal eddy term into its three MSE components (Figure 1d) shows that the
138 geopotential convergence term is also negligible, which is not surprising since pressure levels are
139 close to horizontal at a given latitude. Attempts to compute the vertical eddy term fail however,
140 yielding unrealistically large values likely due to problems with local mass balance arising from the
141 interpolation to pressure coordinates and from errors in the analysis itself which produce unphysical
142 large-amplitude noise in the ω' field (Trenberth 1991).

143 Given these results, we make the following approximations: (i) neglect the MMC term; (ii)
144 neglect the geopotential component of the MSE convergence; (iii) neglect the vertical eddy term.
145 Approximation (iii) cannot be directly justified from our observational analysis, but will be validated
146 a posteriori as discussed below. With these approximations, our final expression for the polar-mean
147 advective heating rate becomes simply

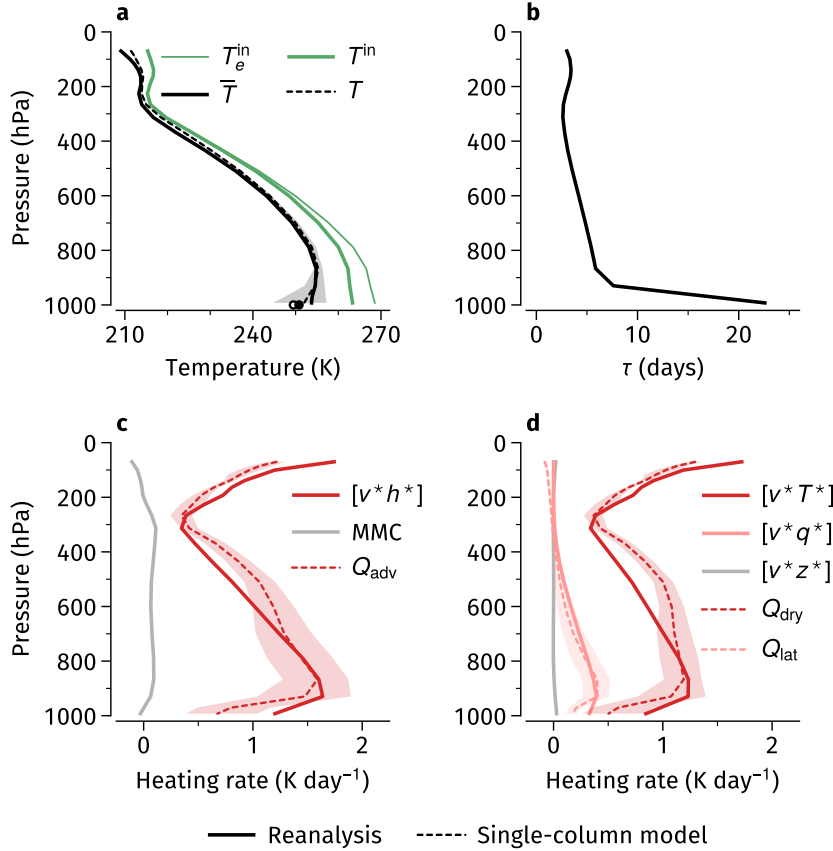
$$\bar{Q}_{\text{adv}} \approx -\frac{v^{\text{in}}}{L} (T_e^{\text{out}} - T_e^{\text{in}}) = -\frac{1}{\tau} (T_e^{\text{out}} - T_e^{\text{in}}) \quad (8)$$

154 where

$$T_e = T + \frac{\ell_v}{c_p} q \quad (9)$$

155 is approximately the equivalent temperature at fixed pressure.

156 The two expressions on the r.h.s. of (8) yield two interpretations. From an Eulerian perspective,
157 (8) can be seen as a coarse-grained advection, with a wind v^{in} acting on a gradient $(T_e^{\text{out}} - T_e^{\text{in}})/L$.
158 From a Lagrangian, air-mass transformation perspective, τ is a residence time—the typical time



143 FIG. 1. (a) Temperatures, (b) residence time τ and (c,d) advective heating rates for the polar cap bounded by
 144 65°N latitude. In all panels, solid lines show climatologies computed from the ERA-Interim reanalysis for winter
 145 (December-February) of 1980-2018, dotted lines show steady-state results for a single-column model simulation
 146 using the reanalysis T_e^{in} and τ profiles in (a,b) as input. In (a), dots along the bottom show surface temperature
 147 in reanalysis (filled) and model (hollow). Shading in (a), (c) and (d) shows an uncertainty envelope due to model
 148 parameter sensitivity (see text).

159 taken for an air parcel to cross the polar cap (note that L is roughly the diameter of the cap).
 160 Figure 1b shows $\tau \sim 5$ days at 800-900 hPa, consistent with the crossing timescale found in
 161 Lagrangian studies (Woods and Caballero 2016). Air parcels enter the polar cap with equivalent
 162 temperature T_e^{in} , travel isobarically while cooling radiatively and diffusively for a time τ , and exit
 163 with the smaller equivalent temperature T_e^{out} ; the rate of energy convergence is proportional to the
 164 resulting energy drop. Both perspectives are equally valid, but we will emphasize the air-mass

165 transformation perspective here since it makes explicit the tight connection between lateral energy
 166 convergence and diabatic cooling within the polar column.

167 *b. Model implementation*

168 We specify the single-column model as

$$\partial_t T = \underbrace{Q_{\text{rad}} + Q_{\text{dif}}}_{Q_{\text{dia}}} + \underbrace{Q_{\text{dry}} + Q_{\text{lat}}}_{Q_{\text{adv}}} \quad (10)$$

169 where T is a prognostic temperature profile controlled by the diabatic cooling rate $Q_{\text{dia}} = Q_{\text{rad}} + Q_{\text{dif}}$
 170 and the advective heating rate $Q_{\text{adv}} = Q_{\text{dry}} + Q_{\text{lat}}$. Using (8) and taking the outflow temperature
 171 T^{out} as the column temperature T , we obtain

$$Q_{\text{dry}} = -\frac{1}{\tau} (T - T^{\text{in}}), \quad Q_{\text{lat}} = -\frac{1}{\tau} \frac{\ell_v}{c_p} (q - q^{\text{in}}) \quad (11)$$

172 where T^{in} and q^{in} are prescribed inflow temperature and specific humidity, while q is the specific
 173 humidity in the column. There is no prognostic equation for q , which is diagnostically computed
 174 from temperature as $q = \text{RH} q_{\text{sat}}(T)$ where q_{sat} is saturation specific humidity and RH is a prescribed
 175 relative humidity. Equation (11) realises the goal of expressing remote effects on the polar column
 176 as a relaxation to prescribed external temperature and humidity profiles, an approach originally
 177 suggested (though not developed) by Cronin and Jansen (2016).

178 At its lower boundary, the column is coupled to a surface slab of fixed heat capacity c and
 179 temperature T_s :

$$c \partial_t T_s = F_{\text{rad}} + F_{\text{SH}} + F_s \quad (12)$$

180 where F_{rad} is the net surface longwave radiative flux and F_{SH} is the surface sensible heat flux,
 181 computed using the bulk-aerodynamic formulation $F_{\text{SH}} = \gamma(T_0 - T_s)$ where T_0 is atmospheric
 182 temperature at the lowest model level and γ is a fixed exchange coefficient. Surface latent heat flux
 183 is neglected because it is very small at the low temperatures considered here ($T_s < 260$ K in all
 184 cases). As in previous work (Payne et al. 2015; Henry et al. 2021), we include a prescribed surface
 185 energy source F_s to represent absorbed surface insolation, ocean energy convergence into the slab,
 186 or the sum of both.

187 Radiative fluxes and cooling rate Q_{rad} are computed using the longwave radiative transfer scheme
 188 of the NCAR CAM3 model (Collins et al. 2004), with only water vapor and CO_2 as radiatively-
 189 active gases. We assume clear-sky conditions and neglect atmospheric solar absorption. Turbulent
 190 fluxes and heating rate Q_{dif} are computed using a simple diffusive scheme with fixed diffusivity
 191 applied to potential temperature, as described in Caballero et al. (2008). Humidity diffusion is not
 192 implemented since q is entirely controlled by temperature and relative humidity.

193 The complete model is implemented in practice using the CliMT framework (Monteiro and
 194 Caballero 2016; Monteiro et al. 2018, we use the “classic” version here). The column is discretized
 195 into 26 levels using the native CAM3 model grid (Collins et al. 2004), which is non-uniform in
 196 pressure with more tightly spaced levels near the surface, improving resolution in the boundary
 197 layer. The model is time-marched until the temperature profile reaches steady state, and all results
 198 shown below refer to this steady state. Note that all simulations presented here do in fact converge
 199 to a fixed point and show no oscillatory or chaotic behavior.

200 *c. Design of simulations and forcing-feedback decomposition*

201 To define a simulation, the following parameters need to be specified: inflow equivalent tem-
 202 perature T_e^{in} , residence time τ , CO_2 concentration (specified in the radiative scheme), surface heat
 203 source F_s , relative humidity RH, kinematic diffusivity κ for the turbulence scheme, and surface
 204 exchange coefficient γ . All simulations here use $\gamma = 6.55 \text{ W m}^{-2} \text{ K}^{-1}$ and a vertically uniform
 205 $\text{RH} = 80\%$. Diffusivity follows an exponentially-decaying profile $\kappa = \kappa_s \exp(-(p_s - p)/\Delta p)$ with a
 206 surface value $\kappa_s = 1 \text{ m}^2 \text{ s}^{-1}$ and a decay rate $\Delta p = 400 \text{ hPa}$; this is done to avoid excessive diffusion
 207 around the tropopause. Other parameters vary as described below.

208 To explore the model’s basic physics, we define a set of simulations using simplified settings: τ
 209 is vertically uniform, and T_e^{in} is specified by defining T^{in} as a profile with a constant lapse rate of
 210 6 K km^{-1} from a surface temperature T_0^{in} up to an isothermal stratosphere at 210 K, and q^{in} is the
 211 corresponding specific humidity assuming $\text{RH} = 80\%$. We define the following simulations:

- 212 • A base simulation \mathcal{B} , intended to represent the preindustrial polar climate, with $\text{CO}_2 =$
 213 280 ppm , $T_0^{\text{in}} = 0^\circ\text{C}$ (the observed annual-mean surface temperature at around 60°N), $F_s =$
 214 50 W m^{-2} (roughly the annual-mean absorbed surface solar radiation averaged over the cap
 215 poleward of 60°N), and $\tau = 10$ days.

- 216 • A perturbed simulation \mathcal{P} , intended to represent the effects of a global doubling of CO_2 , with
 217 $\text{CO}_2 = 560$ ppm and T_0^{in} increased by 3 K from the base state, consistent with central estimates
 218 of global climate sensitivity to a doubling of CO_2 . Changes in surface heat source F_s are
 219 a proxy for sea ice feedback in this model. For guidance, Arctic surface albedo feedback
 220 is estimated at $\sim 3 \text{ W m}^{-2}$ per K of global warming in climate models (Andry et al. 2017),
 221 suggesting $\Delta F_s = 10 \text{ W m}^{-2}$ is an appropriate round-number value for this perturbation.
 222 Changes in τ depend on subtle changes in atmospheric dynamics which are difficult to specify
 223 a priori, so we simply leave it unchanged.

- 224 • A set of single-perturbation simulations $\{\mathcal{P}_{\text{in}}, \mathcal{P}_s, \mathcal{P}_{\text{CO}_2}, \mathcal{P}_q\}$ where the perturbations of \mathcal{P}
 225 are applied one at a time. These simulations are intended to provide a forcing-feedback
 226 decomposition of the change from \mathcal{B} to \mathcal{P} , as done in Henry et al. (2021). They are conducted
 227 with humidity held fixed: in $\mathcal{P}_{\text{CO}_2}$, \mathcal{P}_{in} , and \mathcal{P}_s the temperature is allowed to respond to
 228 increased CO_2 , T_e^{in} , and F_s respectively, but q is held fixed at its value in \mathcal{B} . To evaluate the
 229 water vapor feedback, \mathcal{P}_q has humidity fixed at its value in \mathcal{P} . Water vapor plays a dual role in
 230 the model, affecting both radiative cooling Q_{rad} and latent heating Q_{lat} (see Eq. (11)). These
 231 roles are decoupled in the partial perturbation runs: humidity is fixed only in the radiation
 232 component, so as to isolate the purely radiative water vapor feedback.

233 *d. Testing the model against reanalysis*

234 To test the model’s skill in reproducing observed temperature and heating profiles, we define
 235 a set of simulations aiming to capture the modern Arctic climate. The simulations are identical
 236 to the base simulation \mathcal{B} above, except that T_e^{in} and τ are taken from reanalysis (profiles shown
 237 in Figure 1a,b), and CO_2 is set to 370 ppm, a typical value for the 1980-2018 period covered
 238 by the reanalysis data. To estimate sensitivity to uncertain parameters, we conduct an ensemble
 239 of simulations varying F_s , RH and κ_s in the ranges 40–60 W m^{-2} , 60–95% and 0.5–2 $\text{m}^2 \text{s}^{-1}$
 240 respectively.

241 The ensemble mean of these observationally-informed simulations is shown by dashed lines
 242 in Figure 1, where they can be directly compared with corresponding reanalysis climatologies
 243 (solid lines). Shading shows an uncertainty envelope (minimum-maximum range within the
 244 ensemble). The model reproduces the structure and magnitude of the temperature profile well

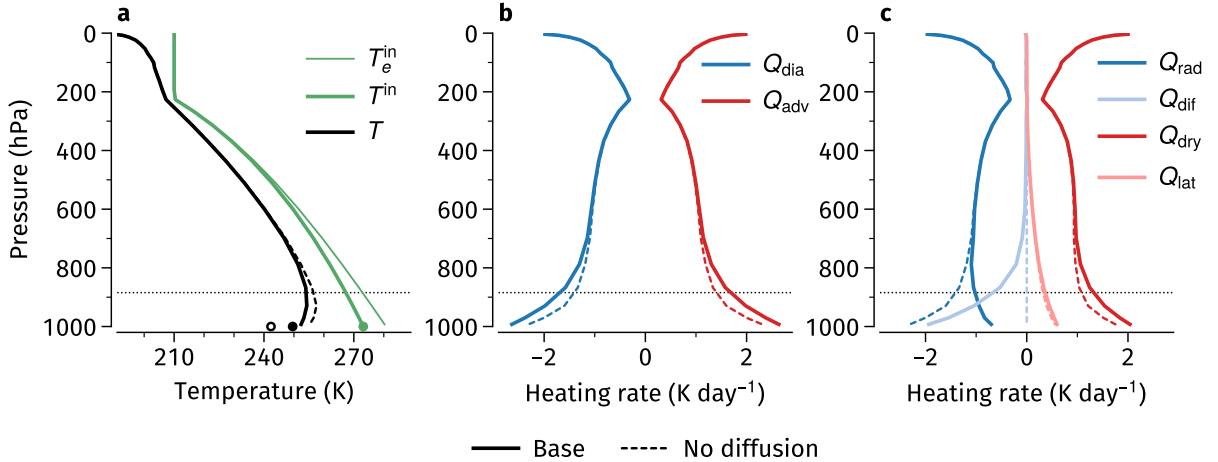
(Figure 1a), though the surface inversion is sensitive to parameters and disappears for high F_s and high diffusivity cases. There is also a good qualitative match to the advective heating rate (Figure 1c), in particular capturing the peak at around 900 hPa and its decline below that level, though again with some parameter spread. Perhaps most surprisingly, the model also captures the partitioning between dry and latent heating quantitatively well (Figure 1d), despite its very simple treatment of condensation. The reasonable match to observations provides a posteriori justification for the neglect of eddy vertical transport in the derivation of Eq. (8). However, in view of the model’s simplicity, in particular its assumption of isobaric flow, clear skies and homogeneous surface, its good match to reanalysis is somewhat surprising and may arise from fortuitous cancellation of different effects.

3. Maintenance of the base state and the surface inversion

a. Energy fluxes in the base state

Results for the base simulation \mathcal{B} are shown in Figure 2 (solid lines). The temperature profile (Figure 2a) shows a surface-based temperature inversion similar to that in reanalysis (Figure 1a). The advective heating rate (Figure 2b) has a bottom-heavy structure peaking at the surface, a structure qualitatively similar to that in reanalysis (Figure 1c), except that in reanalysis the peak is at around 900 hPa. We attribute this difference to the different profile of τ , which is vertically uniform in this simulation but increases strongly below the 900 hPa level in reanalysis (Figure 1b). Winds are more sluggish near the surface and tend to recirculate around the Arctic (Papritz et al. 2023), increasing the residence time near the surface. The difference is not crucial, however; we have repeated all the simulations described in this paper using the reanalysis τ profile and find no qualitative changes to our conclusions.

Separating the diabatic cooling rate into its radiative and diffusive components (Figure 2c) shows the latter is dominant near the surface, suggesting that turbulent transport is essential to the near-surface energy balance and temperature structure. This is not the case, however: repeating simulation \mathcal{B} with diffusion deactivated (dashed lines in Figure 2) shows radiative cooling increasing to replace the lost diffusive cooling. Total diabatic cooling changes little, and the temperature inversion persists albeit with a much larger surface discontinuity. The surface

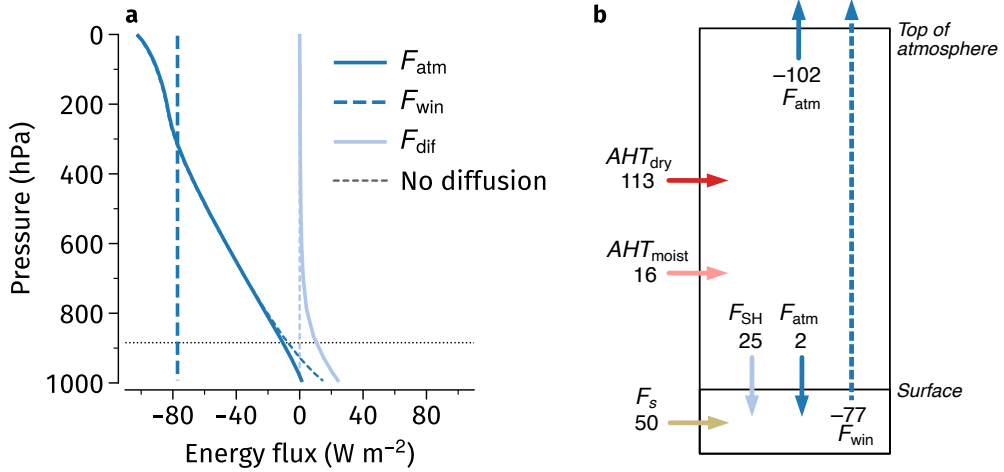


275 FIG. 2. (a) Temperature and (b,c) heating/cooling rate profiles in the base simulation \mathcal{B} , as indicated by the
 276 legend in each panel (solid lines). Dashed lines show results for simulation \mathcal{B} performed with zero diffusivity. In
 277 (a), black dots show surface temperature in the standard (filled) and no-diffusion case (hollow), green dot shows
 278 surface inflow temperature T_0^{in} . Thin dotted lines indicate the zero-flux level.

273 inversion is a robust feature of this base state, independent from whether boundary-layer energy
 274 transfer is dominantly radiative or turbulent.

279 Figure 3a shows the radiative and turbulent energy fluxes whose divergences give the cooling rates
 280 shown in Figure 2c. For reasons that will become apparent later, we have separated the longwave
 281 radiative flux into two streams, F_{atm} and F_{win} . The former consists of radiation absorbed and
 282 emitted by the atmosphere, and is responsible for atmospheric radiative cooling. The latter consists
 283 of radiation emitted by the surface which escapes directly to space, largely in the wavelength range
 284 of the water-vapor window. We estimate the value of F_{win} as outlined in the Appendix, and take
 285 F_{atm} as the difference between F_{win} and the total radiative flux output by the radiation scheme.

286 Under the dry, clear-sky conditions of this simulation, F_{win} is large and accounts for almost half
 287 of the outgoing longwave radiation. F_{atm} is everywhere upward while F_{dif} is downward; their sum
 288 crosses zero around 900 hPa, with net downward energy transport below this level. The zero-flux
 289 level coincides with the top of the temperature inversion (dotted line in Figure 2a), implying that
 290 in the inversion layer the atmosphere is cooling primarily by energy transfer to the surface, rather



293 FIG. 3. (a) Radiative and diffusive energy fluxes, defined positive downwards, in the base simulation \mathcal{B}
 294 (solid and thick dashed lines, see text for definitions). Thin dashed lines show the corresponding fluxes in the
 295 no-diffusion simulation. (b) Column energy budget in \mathcal{B} . All fluxes in W m^{-2} , vertical fluxes defined positive
 296 downward.

291 than to space. The same is true in the no-diffusion case, but the downward flux to the surface is
 292 entirely carried by radiation (dashed lines in Figure 3a).

297 Figure 3b shows the bulk energy budget for the atmospheric column. Dry atmospheric heat
 298 transport convergence, computed as

$$AHT_{\text{dry}} = \frac{c_p}{g} \int_0^{P_s} Q_{\text{dry}} dp, \quad (13)$$

299 is the dominant contributor, with a smaller contribution from moist transport AHT_{moist} (defined
 300 similarly but with Q_{lat} replacing Q_{dry}). This convergence is mostly balanced by 102 W m^{-2}
 301 emission to space, but also by a 27 W m^{-2} flux from the atmosphere to the surface. In turn, the
 302 energy absorbed by the surface from both the atmosphere and from the surface heat source F_s is
 303 emitted directly to space through F_{win} .

304 *b. The surface radiator fin*

305 The above analysis of base-state energy fluxes, schematized in Figure 11a, shows that the near-
 306 surface atmosphere cools primarily by ceding energy to the surface. This is a kind of shortcut:

307 instead of cooling by direct emission to space, the near-surface atmosphere cools by transferring
 308 energy to the surface, which the surface then emits to space via F_{win} . We refer to this as the “surface
 309 radiator fin” effect. The radiator fin analogy was introduced by Pierrehumbert (1995) to describe a
 310 situation where one part of the atmosphere is cooled by energy transfer to another part (the radiator
 311 fin) where it can be efficiently emitted to space. In this sense, the surface serves as a radiator fin
 312 for the near-surface atmosphere in the base state. Note that the radiator fin picture only emerges
 313 if F_{win} is subtracted from the surface longwave flux. The total longwave+turbulent surface energy
 314 flux is *upward* and equal to the surface heat source F_s (Fig 3b), which would naively suggest that
 315 the surface is warming the atmosphere.

316 *c. Conditions for the existence of a surface temperature inversion*

317 In order for the surface radiator fin to exist, a surface-based temperature inversion must also exist:
 318 the near-surface atmosphere must be warmer than the surface, otherwise an atmosphere-to-surface
 319 energy flux would be thermodynamically impossible. Thus the radiator fin and the surface-based
 320 inversion go hand in hand. Ultimately, they both result from the coexistence of strong atmospheric
 321 advective heating with strong surface radiative cooling to space through the optically-thin clearsky
 322 atmosphere. This combination has long been recognized as the cause of *transient* surface-based
 323 inversions in polar regions (Wexler 1936; Curry 1983); the only difference here is that we are
 324 taking a climatological perspective.

325 Under what conditions will a climatological surface inversion and a surface radiator fin form in
 326 our model? To answer this question, we first define a surface temperature T_s^* which would balance
 327 the surface heat source F_s in the absence of warming by energy transfer from the atmosphere:
 328 $w\sigma T_s^{*4} = F_s$ where w is the fraction of the surface upward radiation emitted directly to space and
 329 measures the effective width of the water vapor window. The value of w can be diagnosed as
 330 $w = F_{\text{win}}/\sigma T_s^4$. In the base state we find $w = 0.35$, comparable to Cronin and Jansen (2016)’s
 331 suggested 0.25 for clear-sky conditions

332 We can then define the quantity

$$D = \langle T_e^{\text{in}} \rangle - T_s^* = \langle T_e^{\text{in}} \rangle - \left(\frac{F_s}{w\sigma} \right)^{1/4} \quad (14)$$

355 TABLE 1. Effective water vapor window width w and potential inversion strength D (Eq. 14) in the base
 356 simulation (first column), and their change in perturbed simulations (remaining columns).

	\mathcal{B}	\mathcal{P}_{in}	\mathcal{P}_s	$\mathcal{P}_{\text{CO}_2}$	\mathcal{P}_q	\mathcal{P}
w	0.35	0.00	0.00	-0.01	-0.02	-0.03
D (K)	53	5	-10	-2	-3	-10

333 where $\langle \cdot \rangle$ is an average over the 900–1000 hPa layer. We refer to D as the “potential inversion
 334 strength”: it is the maximum possible surface inversion strength, which would be realised only
 335 if air flowing in from midlatitudes crossed the polar cap without ceding energy to the surface or
 336 cooling to space (and all its latent heat were released).

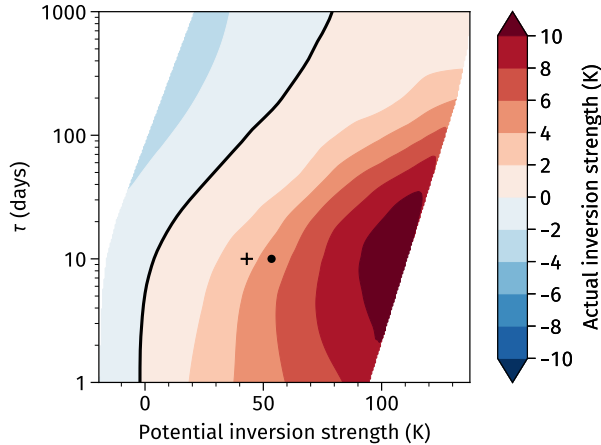
337 In reality, of course, atmosphere-to-surface energy transfer will reduce the actual steady-state
 338 inversion strength to some value less than D . Nonetheless, $D > 0$ provides a *necessary condition*
 339 for the existence of a temperature inversion. On the basis of (14), we expect that an inversion will
 340 exist only if $D > 0$, and will strengthen at small F_s and large w —i.e., for small absorbed insolation
 341 and weak atmospheric opacity. However, $D > 0$ is not a *sufficient* condition for the existence of
 342 an inversion: if the residence time τ is too long (i.e. if midlatitude air is resupplied too slowly),
 343 near-surface air will have time to equilibrate with the surface and the inversion will disappear even
 344 if $D > 0$. We expect the inversion to disappear as τ increases. When $\tau \rightarrow \infty$, advective heating
 345 ceases and the system settles into pure radiative equilibrium, which has no inversion.

346 To test these expectations, we repeat the base simulation with τ and F_s spanning a broad range.
 347 Results (Figure 4) confirm that a surface inversion only forms if $D > 0$, strengthens with increasing
 348 D , and disappears at high τ . Given these results, we expect that any perturbation that increases D ,
 349 such as a warming of the inflow, will increase the strength of the inversion, while an increase in
 350 F_s or a narrowing of the water vapor window will weaken the inversion. These expectations are
 351 tested in the next section.

357 4. Response to perturbations

358 a. Lapse rate

359 When the base state \mathcal{B} is perturbed by a simultaneous increase of T^{in} , CO_2 , and F_s to yield
 360 the perturbed state \mathcal{P} , the temperature warms throughout the troposphere with a bottom-heavy

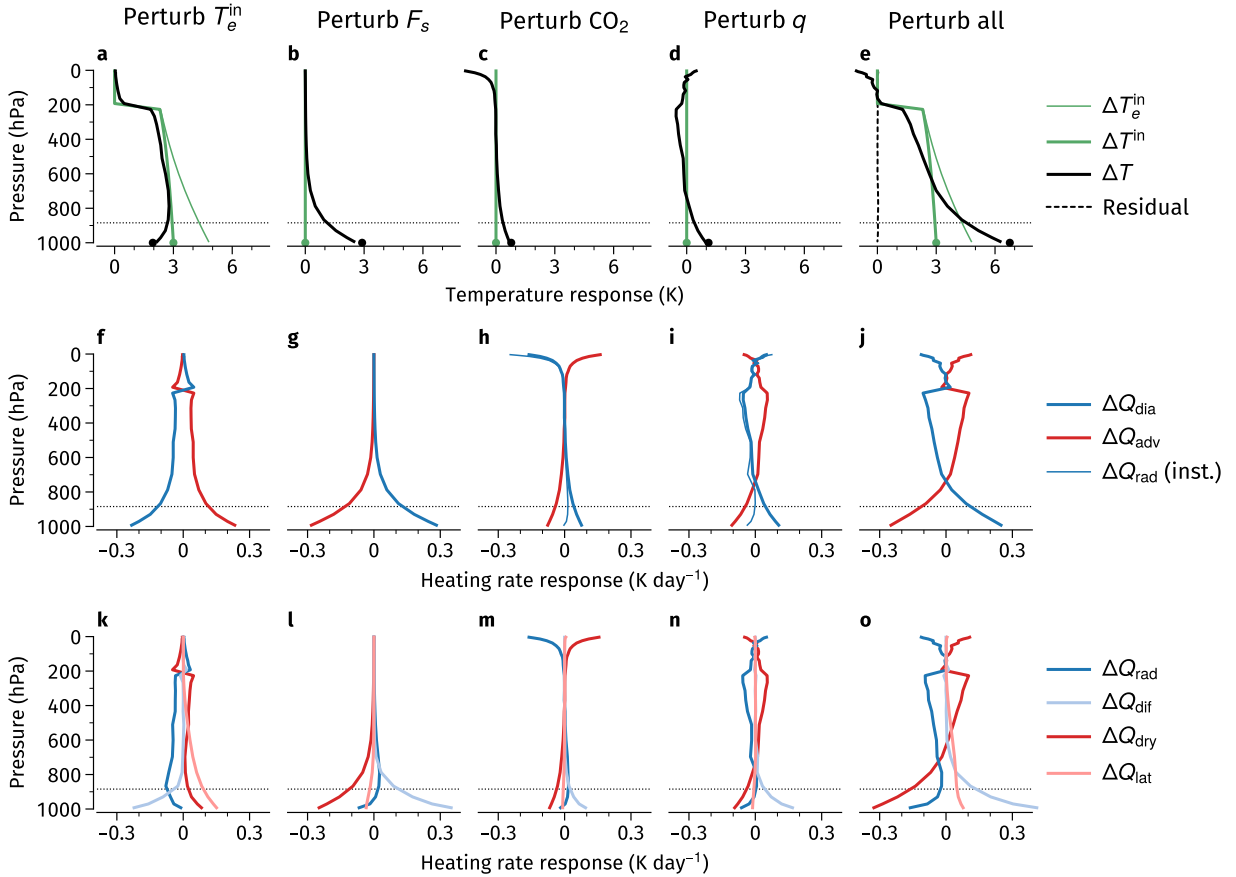


352 FIG. 4. Surface temperature inversion strength (measured as maximum temperature in the 800–1000 hPa layer
 353 minus surface temperature) as a function of potential inversion strength D and residence time τ . Dot and cross
 354 show values for simulations \mathcal{B} and \mathcal{P} respectively.

361 structure (Figure 5e). Comparing this response to the change in inflow temperature T^{in} (thick
 362 green line) gives a measure of the polar amplification between midlatitudes and the pole. Polar
 363 amplification is strong in the lower troposphere but negative at upper levels, where the pole warms
 364 less than midlatitudes. These features agree with the results of comprehensive climate models
 365 subject to global forcing (Previdi et al. 2021; Taylor et al. 2022),

366 To understand the origins of this general destratification of the polar atmosphere, we examine
 367 the single-perturbation simulations \mathcal{P}_{in} , \mathcal{P}_s , $\mathcal{P}_{\text{CO}_2}$ and \mathcal{P}_q . They provide a forcing-feedback
 368 decomposition of the total response with near-zero residual (dashed line in Figure 5e), implying
 369 the decomposition is almost perfectly linear. In the following paragraphs we examine each of the
 370 perturbations in turn, starting with the response to increased surface heat source (\mathcal{P}_s), moving on
 371 to greenhouse gases ($\mathcal{P}_{\text{CO}_2}$ and \mathcal{P}_q), and ending with the response to inflow warming (\mathcal{P}_{in}).

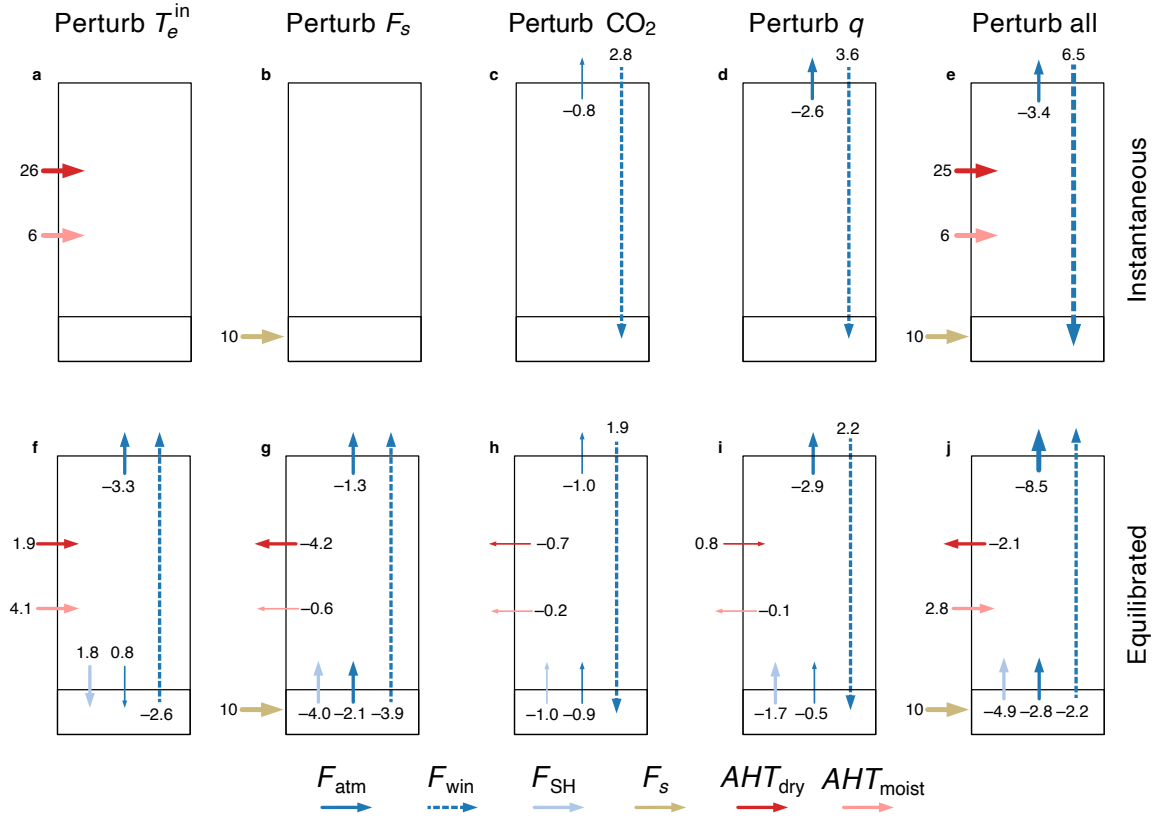
372 The temperature response to increased F_s is strongly bottom-amplified in the lower troposphere
 373 and negligible above ~ 600 hPa (Figure 5b), implying a strong reduction in inversion strength and
 374 confirming our expectations based on the radiator fin picture of the previous section: increasing F_s
 375 reduces potential inversion strength D by 10 K (Table 1). Physically, air masses entering the polar
 376 cap now encounter a warmer surface, experience weaker diabatic cooling as they traverse the cap
 377 (Figure 5g), and therefore remain warmer. This effect is strongest in the inversion layer below the



382 FIG. 5. Changes in temperature (top row) and heating/cooling rates (middle and bottom rows) from base
 383 simulation \mathcal{B} to perturbed simulation \mathcal{P}_{in} (first column), \mathcal{P}_s (second column), \mathcal{P}_{CO_2} (third column), \mathcal{P}_q (fourth
 384 column) and \mathcal{P} (fifth column). Dots in top row show surface temperature change in the inflow (green) and in the
 385 column (black). Dashed line in (e) shows the residual between the sum of individual responses in (a-d) and the
 386 full response in \mathcal{P} . Thin blue lines in (h,i) show the instantaneous response of the radiative cooling rate when
 387 the corresponding perturbation is applied. Thin dotted lines indicate the zero-flux level of the base simulation.

378 zero-flux level, which is directly coupled to the surface, but is communicated some distance upward
 379 by intra-atmospheric radiative and diffusive energy exchange. The upper troposphere experiences
 380 no forcing and remains unaffected. Reduced energy transfer from atmosphere to surface also
 381 implies an *upward* anomaly in surface radiative and turbulent fluxes (Figure 6g).

388 Turning to greenhouse gas forcing in \mathcal{P}_{CO_2} and \mathcal{P}_q (Figure 5c,d), we see in both cases a bottom-
 389 amplified structure similar to that in \mathcal{P}_s , in agreement with previous work (Lu and Cai 2010; Henry
 390 et al. 2021). The instantaneous effect of increasing either CO_2 or H_2O concentrations is to render



399 FIG. 6. Instantaneous (top row) and equilibrated (bottom row) perturbation energy budget for the change from
 400 base simulation \mathcal{B} to perturbed simulation \mathcal{P}_{in} (first column), \mathcal{P}_s (second column), $\mathcal{P}_{\text{CO}_2}$ (third column), \mathcal{P}_q
 401 (\mathcal{P} (fifth column)). Thick arrows show changes $> 1 \text{ W m}^{-2}$, thin arrows $< 1 \text{ W m}^{-2}$.

391 previously transparent wavelengths opaque, blocking direct surface emission to space within a
 392 certain wavelength range (Jeevanjee et al. 2021; Seeley and Jeevanjee 2021; Koll et al. 2023). The
 393 result is an effective narrowing of the water vapor window. This leads to an instantaneous decrease
 394 in surface cooling by F_{win} (Figure 6c,d) and thus a warming tendency on the surface (consistent
 395 with a surface vs. atmosphere decomposition of reanalysis-based CO_2 forcing for Earth’s Arctic,
 396 Chen et al. 2023, their Figs. 10a,b). Hence the similarity between the response to greenhouse gases
 397 and to direct surface warming by F_s : they both weaken D (Table 1), making the surface radiator
 398 fin less efficient albeit by different mechanisms.

402 Differently from F_s , however, increased H₂O and CO₂ provide strong cooling responses in the
403 free troposphere (defined as the layer between ~800 and 300 hPa) and the stratosphere respectively
404 (Fig. 5c,d). This is again in agreement with previous work (Lu and Cai 2010; Henry et al. 2021).
405 Increased CO₂ shifts radiative emission to space from the surface to the stratosphere within a
406 wavelength range on the flanks of the main 15 micron absorption band, causing increased cooling
407 in the stratosphere (Jeevanjee et al. 2021; Chen et al. 2024). Increased H₂O, on the other hand,
408 produces cooling in the upper troposphere and the interpretation is more subtle in this case. H₂O
409 produces radiative cooling to space throughout the troposphere, but the exponential decay of
410 humidity with height implies an abrupt decline of this cooling ability above a height where the
411 water path drops below a critical level (the upper-tropospheric “kink”, Jeevanjee and Fueglistaler
412 2020). This behavior can clearly be seen in Fig. 2c, which shows fairly uniform radiative cooling
413 rates between 800 and 400 hPa and a sharp decrease towards the tropopause at around 250 hPa.
414 The effect of increasing water vapor is to shift this profile upwards, yielding increased cooling
415 rates in the 250–400 hPa layer. This effect is of some importance since it emerges as a key cause
416 of free-tropospheric lapse rate change and of negative upper-level polar amplification, and would
417 be worth exploring further with a more accurate radiative scheme than employed here. The gray-
418 radiation based theory of Cronin and Jansen (2016) also produces a bottom-amplified temperature
419 response to increased atmospheric opacity, but this spectrally-informed picture is more faithful to
420 the balances at upper levels.

421 Finally, we examine the response to increased T_e^{in} . The entire troposphere warms in this case
422 (Figure 5a). Since the T_e^{in} perturbation is itself bottom-heavy (because of greater humidity at low
423 levels), and since the model essentially relaxes T to T_e^{in} (see Section 2b), we expect to see a similar
424 bottom-heavy structure in the T response. This is indeed the case in the free troposphere, where the
425 lapse rate increases somewhat. Upper-tropospheric warming also leads to increased atmospheric
426 cooling to space (top-of-atmosphere F_{atm} increases by 3.3 W m^{-2} , Figure 6f). On the other hand,
427 potential inversion strength increases, enhancing diabatic cooling to the surface (Figure 5f) and
428 strengthening the inversion (Figure 5a). Warming of the inflow increases stratification of the lower
429 troposphere, counteracting the destratifying effect of the other perturbations. Equivalently, this
430 ‘forcing’ is not polar amplified at the surface, with ~2 K warming compared to the imposed 3 K

431 change in T^{in} . Overall, the atmosphere warms more than the surface while advective heating
 432 increases, consistently with previous work (Cai 2005, 2006; Cai and Lu 2007; Lu and Cai 2010)

433 *b. Dry and moist energy convergence*

434 A robust result of climate model simulations subject to global radiative forcing is that changes in
 435 vertically-integrated dry and moist energy transport to the poles compensate each other, yielding
 436 near-zero net change in transport (Hwang et al. 2011). This compensation is understood to
 437 result from opposite changes in temperature and moisture gradients: despite polar amplification,
 438 Clausius-Clapeyron scaling means moisture increases more in midlatitudes than at the poles, so
 439 moist transport increases while dry transport drops (Merlis and Henry 2018; Armour et al. 2019).
 440 This compensation also occurs in our all-perturbations simulation \mathcal{P} , where a $+2.8 \text{ W m}^{-2}$ change
 441 in vertically-integrated moist transport is offset by a -2.1 W m^{-2} change in dry transport (Figure 6j).

442 In the rest of this section, we study how different forcings and feedbacks, and different layers in
 443 the atmospheric column, contribute to this overall compensation. To provide a framework for this
 444 discussion, we use (10) and (11) to write the steady-state perturbation energy budget as

$$\frac{1}{\tau}(\Delta T^{\text{in}} - \Delta T) + \frac{1}{\tau}(\alpha^{\text{in}}\Delta T^{\text{in}} - \alpha\Delta T) = -\Delta Q_{\text{dia}} \quad (15)$$

445 where we have defined the Clausius-Clapeyron factor

$$\alpha(T) = \frac{\ell_v \text{RH}}{c_p} \left. \frac{dq_{\text{sat}}}{dT} \right|_T \quad (16)$$

446 and $\alpha^{\text{in}} = \alpha(T^{\text{in}})$. As shown in Figure 7a, $\alpha \approx 1$ at 270 K and drops by an order of magnitude for
 447 every ~ 20 K drop in temperature.

448 In the upper troposphere, base-state temperatures are below 250 K (Figure 2), and both α and
 449 $\alpha^{\text{in}} \ll 1$. Moisture plays a negligible role, and changes in diabatic heating are entirely balanced by
 450 dry heating: specifically, dry heating increases to balance increased radiative cooling in \mathcal{P}_{in} and
 451 \mathcal{P}_q (Figure 5k,n). Physically, increased radiative cooling causes a larger temperature drop from
 452 inflow to outflow, increasing the dry energy convergence.

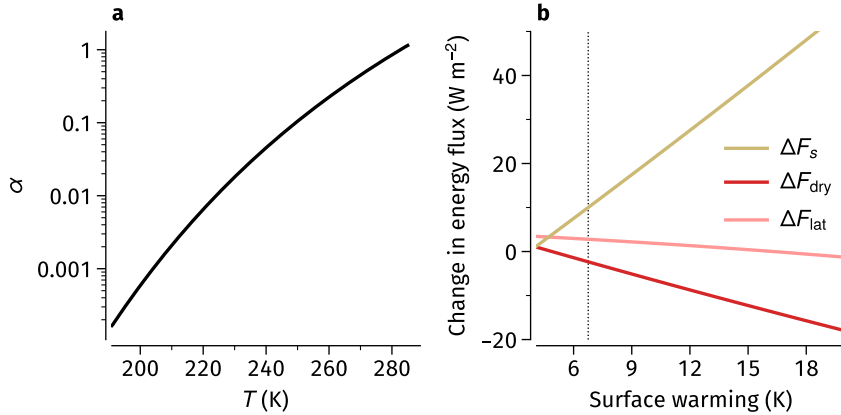
453 In the lower troposphere, on the other hand, $\alpha \ll 1$ but $\alpha^{\text{in}} \sim 1$. In \mathcal{P}_s , \mathcal{P}_q and $\mathcal{P}_{\text{CO}_2}$ there is no
 454 T_e^{in} perturbation, so (15) reduces to $\Delta T/\tau \approx \Delta Q_{\text{dia}}$ and decreased diabatic cooling is again balanced

455 almost entirely by reduced dry heating (Figure 5 l,m,n). Physically, these perturbations warm the
 456 surface and reduce the radiator fin effect. The resulting drop in diabatic cooling results in warmer
 457 outflow temperature and reduced dry convergence, but outflow humidity is hardly affected by the
 458 warming so there is little change in moist convergence. In the \mathcal{P}_{in} case, on the other hand, the
 459 temperature increase in the column roughly matches that of the incoming air, $\Delta T^{\text{in}} \approx \Delta T$ (Figure 5a),
 460 so (15) becomes $\alpha^{\text{in}} \Delta T^{\text{in}} / \tau \approx -\Delta Q_{\text{dia}}$. In this case, increased latent heating balances much of the
 461 increase in diabatic cooling (Figure 5k). Physically, increased inflow temperature increases the
 462 radiator fin effect; the resulting increase in diabatic cooling mostly consumes the increased latent
 463 heat of the inflow air, however, leading to a modest change in inflow-to-outflow temperature drop
 464 and hence in dry advective heating rate. This is reminiscent of the “energy hypothesis” proposed
 465 by Pithan and Jung (2021): increased diabatic cooling in the polar region is balanced mostly by
 466 increased precipitation and latent heating, rather than by increased dry static energy convergence.

467 When added together (Figure 5o), the perturbations give free-tropospheric increase but lower-
 468 tropospheric decrease in dry heating, along with lower-tropospheric increase in latent heating
 469 (contributed entirely by the T_e^{in} perturbation). The vertically-integrated compensation between dry
 470 and moist transports is thus a delicate balance between positive and negative changes at different
 471 levels in the column responding to different physical processes. There is no obvious constraint
 472 imposing exact compensation. It is therefore not surprising that the degree of compensation is
 473 highly variable between climate models (Hwang et al. 2011; Hahn et al. 2021), which have varying
 474 F_s or T^{in} in our framework. Note also that the layer-wise compensation seen in the RAE single-
 475 column model cannot be captured in energy balance models, which parameterize all transport
 476 down moist- or dry-energy gradients based on surface temperature only (e.g., Feldl and Merlis
 477 2021; Chang and Merlis 2023).

478 Moreover, the degree of compensation is sensitive to the surface heat source perturbation ΔF_s .
 479 If we repeat simulation \mathcal{P} but varying ΔF_s in the range 0–50 W m^{-2} , we find that dry transport
 480 decreases strongly while moist transport stays roughly constant as ΔF_s increases (Figure 7b). This
 481 happens because the negative contribution to dry heating given by the F_s perturbation grows
 482 while leaving latent heating largely unaffected (Figure 5l). Recalling that ΔF_s represents sea ice
 483 feedback in our model, we note that this result provides an explanation for the negative correlation

484 between the strength of surface albedo feedback and atmospheric energy transport in climate model
 485 intercomparisons (Pithan and Mauritsen 2014; Hahn et al. 2021, their Figure 6).

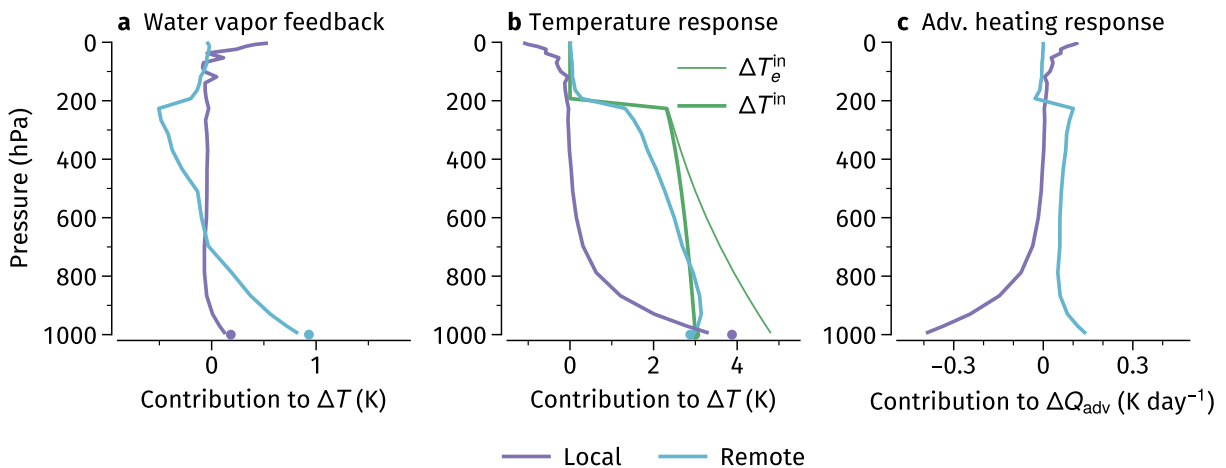


486 FIG. 7. (a) Behavior of the non-dimensional Clausius-Clapeyron factor α (see Eq. 16) as a function of
 487 temperature, assuming RH=80% and a pressure of 1000 hPa. (b) Behavior of the dry and moist advective heating
 488 perturbations in response to changing surface heat source perturbation, plotted as a function of surface warming.

489 5. Local and remote contributions to polar warming

490 Polar warming is driven by a combination of remote and local forcing, both amplified by local
 491 feedbacks (Screen et al. 2012; Stuecker et al. 2018; Park et al. 2018; Henry et al. 2021). Here,
 492 we partition the total warming seen in the all-perturbations simulation \mathcal{P} into remote and local
 493 contributions. Remote forcing in our model is encapsulated in the T_e^{in} perturbation. We take
 494 the remote warming contribution to be the sum of the direct response to this forcing (given by
 495 simulation \mathcal{P}_{in}), and the portion of the water vapor feedback driven by remote warming (Henry
 496 et al. 2021). We quantify this portion by performing an additional simulation identical to \mathcal{P}_{in}
 497 but allowing water vapor to adjust interactively at fixed RH. Local forcing is provided by the
 498 CO_2 and F_s perturbations, both amplified by corresponding portions of the water vapor feedback
 499 (again quantified by additional simulations). The F_s perturbation can be seen as this model's
 500 representation of sea ice feedback, which could be partly driven by remote warming. Nonetheless,
 501 we treat F_s as a purely local effect for consistency with previous work (Henry et al. 2021), while
 502 recognizing that this assumption overestimates the local contribution to total warming.

503 Results are presented in Figure 8. Partitioning of the water vapor feedback shows that it is almost
 504 entirely due to remote warming (Figure 8a), presumably because this warming is deep and promotes
 505 enhanced humidity throughout the column rather than in a near-surface layer. (Consistently with
 506 this argument, we also note that water vapor radiative kernels have small or even negative near-
 507 surface values in the Arctic because of the climatological inversion, implying modest changes in
 508 outgoing longwave radiation for increased near-surface specific humidity (Soden et al. 2008; Kim
 509 et al. 2021).) With this contribution from water vapor feedback, surface warming attributed to
 510 remote forcing becomes comparable to that attributed to local forcing (Figure 8b). These results
 511 confirm that remote forcing plays a key role in driving strong polar amplification: if remote forcing
 512 had no effect on the poles, there would be very weak polar amplification.



513 FIG. 8. Decomposition of the (a) radiative water vapor feedback, (b) total temperature response, and (c)
 514 advective heating rate response into contributions due to local and remote forcings/feedbacks.

515 Remote forcing also drives increased advective heating—and therefore increased diabatic
 516 cooling—throughout the troposphere, while local forcing is responsible for the net drop in advective
 517 heating in the lower troposphere (Figure 8c). This result is consistent with and helps interpret
 518 the findings in Audette et al. (2021), who examine the response of atmospheric energy transport and
 519 moist-isentropic circulation in atmospheric models subject to changing surface conditions. They
 520 find that remote sea-surface temperature warming leads to greater energy transport to the Arctic and
 521 greater isentropic mass flux. Both are consistent with the remote response in Figure 8c—note in
 522 fact that the poles constitute the subsiding branch of the isentropic circulation (Pauluis et al. 2010),

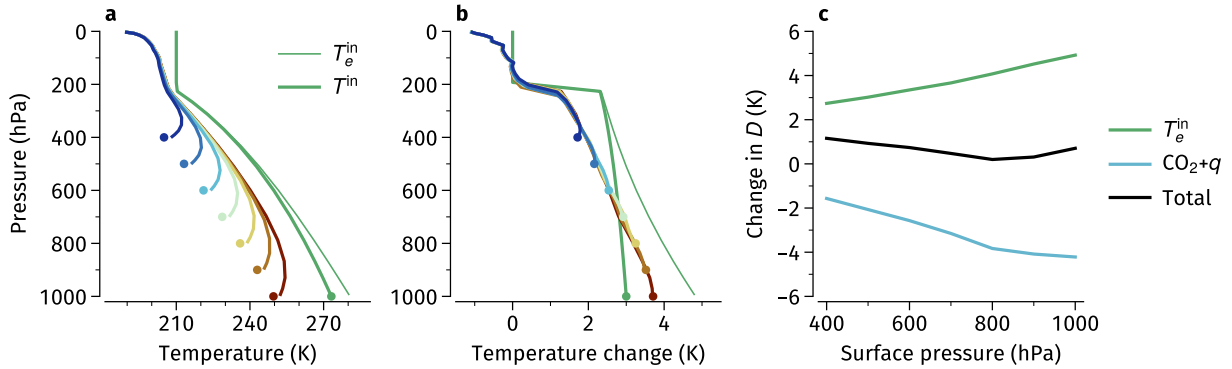
523 and in isentropic coordinates subsidence is equal to the diabatic cooling rate and related moisture
524 loss by precipitation (it is simply the transformation of air masses from higher to lower entropy
525 or MSE classes). This isentropic picture also forms the basis of a feedback analysis suitable to
526 separating the distinctive upper- vs. lower-tropospheric warming contributions in the Arctic (Feldl
527 et al. 2020). Audette et al. (2021) further show that local polar forcing by reduced sea ice cover
528 drives reduced energy transport and a weakening of the isentropic mass transport in the lower tro-
529 posphere; both are again consistent with our results for local forcing, for the same physical reasons.
530 Moreover, they attribute this reduction in energy transport to warming of the low-level outflow
531 from the Arctic, consistent with the air-mass transformation perspective discussed in Section 4b.
532 In summary, our single-column model results suggest that changes in poleward energy transport
533 and in isentropic mass flux are just two sides of the same coin.

534 **6. Sensitivity to surface elevation: The Antarctic case**

535 Polar amplification is hemispherically asymmetric, being stronger over the Arctic than over
536 Antarctica. This asymmetry has been attributed in part to Antarctica’s high elevation: climate
537 model simulations in which Antarctica is flattened with no change in surface albedo show substan-
538 tially increased polar amplification (Salzmann 2017; Hahn et al. 2020).

539 This issue provides a useful test case for the single-column model and for the physical picture
540 developed in Sections 3 and 4. We perform a series of simulations identical to \mathcal{B} but with varying
541 surface pressure. The T_e^{in} profile prescribed in these simulations is identical to the portion of the
542 T_e^{in} profile of \mathcal{B} that is above the surface. The resulting series of base-state temperature profiles is
543 shown in Figure 9a. In agreement with Hahn et al. (2020), the surface inversion becomes stronger
544 but shallower as the surface pressure decreases.

549 We then perform a corresponding series of perturbed simulations which are identical to \mathcal{P} with
550 one exception: the surface heat source perturbation $\Delta F_s = 0$ in all cases, to mimic no change
551 in surface albedo. Profiles of temperature change from corresponding base states are shown in
552 Figure 9b. The lapse rate increases roughly uniformly throughout the column in these simulations,
553 without the lower-tropospheric enhancement seen in \mathcal{P} (Figure 5e). The reason is that without an
554 F_s perturbation, the reduction in potential inversion strength D due to greenhouse gases roughly
555 cancels out the increase due to T_e^{in} (Figure 9c). There is therefore little change in radiator fin



545 FIG. 9. (a) Base-state temperatures and (b) temperature response to perturbed T_e^{in} and CO_2 for simulations with
 546 varying surface pressure. Dots show surface temperature, plotted at the corresponding value of surface pressure.
 547 (c) Change in potential inversion strength D from the base to the perturbed simulations as a function of surface
 548 pressure (black line), and its partitioning into contributions from increased T_e^{in} and in greenhouse gases.

556 strength, implying that near-surface lapse-rate changes in these simulations are not primarily due
 557 to the boundary-layer processes that control the surface inversion strength. Instead, lapse-rate
 558 changes are driven by relaxation towards the bottom-amplified T_e^{in} perturbation—note that the T
 559 perturbation profile is roughly parallel to that of T_e^{in} in Figure 9b—and by upper-tropospheric
 560 cooling by water vapor as discussed in Section 4a.

561 In summary, these results show that the model’s surface temperature response decreases with
 562 increasing surface elevation, in agreement with the climate model results of Salzmann (2017) and
 563 Hahn et al. (2020). Our physical interpretation is different from theirs, however, and points to the
 564 importance of lower-tropospheric latent heat release in yielding a bottom-amplified temperature
 565 response which enhances polar amplification.

566 7. Comparison with other forcing-feedback decompositions

567 Here we compare the forcing-feedback decomposition provided by our relaxation approach with
 568 alternative decompositions provided by the fixed-heating RAE approach (Henry et al. 2021) and
 569 by the conventional TOA decomposition. For the fixed-heating approach, we perform simulations
 570 with the same parameter settings specified in Section 2c, but prescribing a fixed advective heating
 571 rate diagnosed from simulations \mathcal{B} and \mathcal{P} . For the TOA decomposition, we use the partial radiative
 572 perturbation method (Colman et al. 2001): using the radiative transfer code offline, we compute the

573 TOA radiative perturbation caused by replacing temperature, humidity and CO₂ values in \mathcal{B} with
574 those from \mathcal{P} one at a time; we then divide by the Planck feedback to obtain as surface temperature
575 change contribution from each feedback. Contributions from changes in surface heat source and
576 atmospheric heat transport are computed by dividing ΔF_s and vertically-integrated ΔQ_{adv} by the
577 Planck feedback.

578 Results are presented in Figure 10. Temperature responses to F_s , CO₂ and q in the fixed-
579 heating approach are qualitatively similar to those in the relaxation approach, but with much
580 greater amplitude: since advective heating is not allowed to adjust, changes in diabatic cooling
581 must be entirely compensated by large temperature changes. Note in particular that the response
582 to F_s is positive all the way into the stratosphere in the fixed-heating approach. Moreover, the
583 negative lower-tropospheric lobe of ΔQ_{adv} (shown in Figure 5j) yields a large negative temperature
584 perturbation even at the surface, although vertically-integrated atmospheric heat transport actually
585 increases. These responses appear more difficult to interpret physically than in the relaxation
586 approach.

587 The TOA decomposition (Figure 10c) shows the largest contribution to surface temperature
588 change is from F_s , followed by lapse-rate feedback, while other terms play a smaller role; in
589 particular, atmospheric transport gives a small positive contribution. This is qualitatively consistent
590 with the relative roles of Arctic surface albedo, lapse-rate and atmospheric transport feedbacks
591 in diagnosed in climate models (Pithan and Mauritsen 2014; Hahn et al. 2021). ΔF_s is also the
592 largest contributor in the relaxation and fixed-heating approaches, though it is much larger in the
593 fixed-heating approach to compensate for the negative contribution from advective heating (recall
594 from Section 4b that ΔF_s drives the largest reduction in Q_{adv}). The two RAE approaches do
595 not have an explicit lapse-rate feedback contribution since it is implicitly partitioned among the
596 other contributions, making the CO₂ and q contributions larger than in the TOA approach. In
597 addition, the relaxation approach has no separate atmospheric transport feedback; instead it has
598 a substantial contribution from ΔT_e^{in} , which we consider a forcing, while changes in atmospheric
599 energy convergence are partitioned among all four contributions.

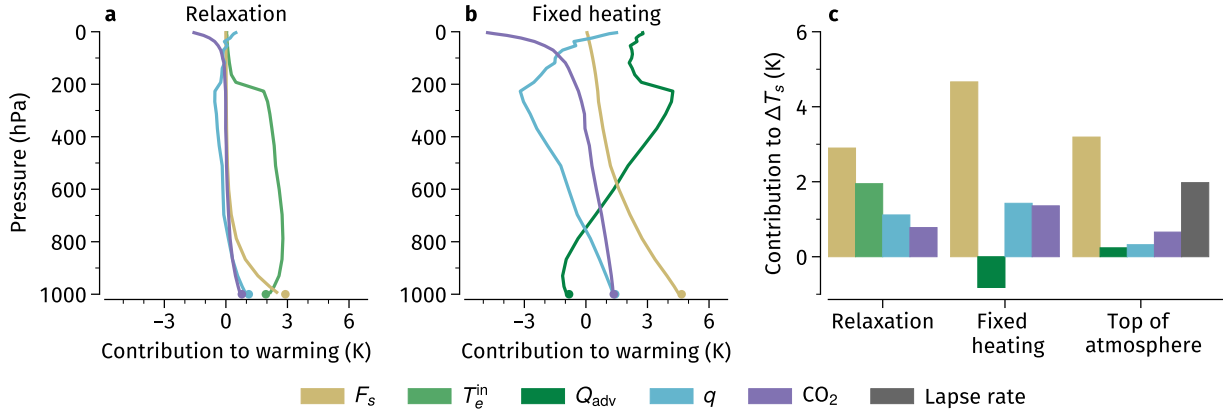


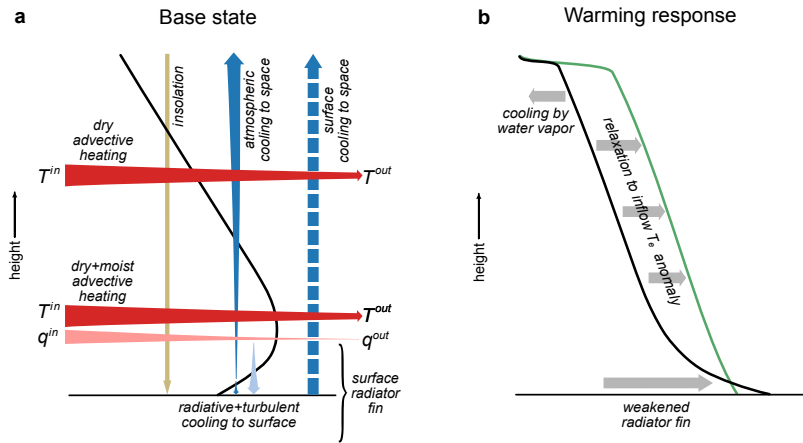
FIG. 10. Temperature responses to individual perturbations in the (a) relaxation and (b) fixed-heating approaches, and (c) contributions to surface temperature change according to the three decompositions. Dots in (a,b) show surface temperature change.

8. Summary and conclusions

We have developed a single-column model for clear-sky RAE in which heating by lateral energy advection is represented as a relaxation toward a fixed midlatitude profile of temperature and humidity, encapsulated in the equivalent temperature profile T_e^{in} . Despite its simplicity, the model adequately reproduces observed Arctic temperature and energy convergence profiles. Analysis of the model's steady-state energy balance, schematized in Figure 11a, and its response to a global-warming-like perturbation (Figure 11b), allows us to provide some answers to the key questions posed in the Introduction:

1. *Why is there a climatological surface-based inversion, and what mechanisms control the polar lapse-rate response to global warming?*

In our model, a climatological surface-based inversion can exist when advective heating keeps the atmosphere sufficiently warm compared to the surface, which cools strongly to space through the radiatively thin atmosphere. This situation arises when two conditions are simultaneously fulfilled: (i) near-surface air flowing into the polar cap is warmer than the surface temperature that would prevail if atmosphere-surface energy exchange were suppressed; this is expressed by the potential inversion strength condition $D > 0$ (see Sec. 2c); (ii) the residence time τ is short enough to prevent thermodynamic equilibration between atmosphere and sur-



611 FIG. 11. Schematics summarizing (a) the energy balances involved in the maintenance of the base state, and
 612 (b) the mechanisms controlling polar lapse rate response to a global warming perturbation. In (a), the black
 613 line indicates the climatological temperature and tapered arrows indicate convergent or divergent energy flows,
 614 emphasizing the difference between the surface inversion layer—where atmospheric cooling is mediated by
 615 energy transfer to the surface and subsequent radiative loss to space (the surface radiator fin)—and in the free
 616 atmosphere, where cooling occurs by direct atmospheric emission to space. In (b), the green line shows the
 617 imposed T_e^{in} anomaly (which is inherently bottom-heavy due to increased latent heat content near the surface),
 618 the black line shows the polar temperature response, and gray arrows indicate warming or cooling tendencies
 619 due to different mechanisms as in noted in the figure.

629 face. Under these conditions, the lower troposphere cools primarily by energy transfer to the
 630 surface; this transfer can be accomplished by radiative or turbulent fluxes interchangeably, but
 631 necessitates a surface temperature inversion in either case. We refer to this surface cooling
 632 mechanisms as the surface radiator fin.

633 Changing inversion strength in response to global-warming-like perturbations can be readily
 634 predicted by thinking about their effects on the surface radiator fin. All else equal, a warming
 635 of incoming air will strengthen the radiator fin and yield a stronger inversion. Vice-versa,
 636 warming the surface through decreased albedo or blocking the water-vapor window by in-
 637 creased greenhouse gas concentration will weaken the inversion. As indicated in Figure 11b,
 638 these changes to the lower-tropospheric temperature structure are superposed on an overall
 639 increase in lapse rate throughout the column due to relaxation toward an equivalent temper-

640 ature perturbation ΔT_e^{in} that is intrinsically bottom-heavy. Furthermore, increasing humidity
641 results in increased upper-level radiative cooling, which tends to further increase the overall
642 lapse rate.

- 643 2. *Why do changes in moist and dry energy transport to the poles tend to mutually compensate,*
644 *and what constraints act to enforce this compensation?*

645 Given typical temperatures in Earth’s modern climate, warming the low-level inflow to the
646 polar caps causes comparable changes in dry and latent energy content of the inflowing air
647 masses, while a similar perturbation to outflow temperature causes a much smaller change in
648 latent energy content. This means that essentially all additional moisture entering the polar cap
649 in a warmed climate will condense and release its latent heat—moist energy convergence can
650 increase, but not decrease in response to warming. On the other hand, the strong reduction of
651 radiator fin strength in response to warming (see point 1 above) requires an overall reduction in
652 energy convergence at low levels, which can only be accomplished by a warming of the outflow
653 and reduced dry energy convergence. Compensation between dry and moist energy transport
654 is therefore a robust, thermodynamically-constrained response at low levels. At upper levels,
655 both inflow and outflow temperatures are low enough that moisture plays a negligible role.
656 Increased upper-level radiative cooling in response to warming is thus balanced by increased
657 dry energy convergence. Overall, the precise degree of compensation between vertically-
658 integrated moist and dry transport depends delicately on radiative responses at different levels
659 and is not robust.

- 660 3. *What is the best way to decompose forcing and feedbacks at the poles?*

661 In agreement with much previous work (Lu and Cai 2009; Cai and Lu 2009; Cronin and Jansen
662 2016; Henry et al. 2021; Feldl et al. 2020; Boeke et al. 2021), our analysis shows that lapse-
663 rate feedback at the poles does not constitute a well-defined standalone mechanism: different
664 forcing and feedback agents affect the lapse rate differently and through disparate mechanisms.
665 More fundamentally, in RAE there is no strong relationship between surface temperature and
666 TOA radiative fluxes, since much of the outgoing longwave radiation originates in the mid-
667 to upper troposphere which is decoupled from the surface. It makes more sense therefore to

668 think only in terms of a temperature profile response which includes a lapse-rate response that
669 is different for each forcing and feedback.

670 We go a step further. We note that polar temperature change is an adjustment to bring
671 changes in diabatic cooling into balance with changes in advective heating. Temperature
672 affects *both* the diabatic and advective sides of this equation. We can therefore think of a
673 generalized temperature feedback which includes both radiative and advective components.
674 Rather than lumping advective feedback into a single, externally-imposed change in advective
675 heating, we argue that it makes more sense to distribute the advective feedback among the
676 responses to other external forcings. These external forcings include local changes in CO₂ and
677 surface albedo, as well and remote forcing represented by warming of the inflow equivalent
678 temperature profile T_e^{in} .

679 We emphasize that the conclusions above are derived exclusively from analysis of our highly
680 simplified model. Though the model shows some qualitative agreement with the behavior of full-
681 complexity models, the general applicability of these conclusions to real-world scenarios requires
682 further careful assessment. Nonetheless, we believe that the model explored here—and the concepts
683 and mechanisms elucidated by this exploration—may provide a useful basic framework for thinking
684 about the polar climate. It is certainly an incomplete framework as it stands. It lacks a description
685 of cloud effects—in particular, high-opacity low-level clouds can be expected to substantially affect
686 the functioning of the surface radiator fin and could strongly affect the surface temperature response
687 (Cronin and Tziperman 2015; Dimitrelos et al. 2023). Our model also assumes a homogeneous
688 surface, lacking a description of partial sea-ice cover and an explicit surface-albedo feedback. This
689 is an important limitation since a heterogeneous surface including leads and open water could alter
690 the surface energy balance substantially and also affect the surface radiator fin. Understanding
691 whether these additional effects lead to qualitatively different behavior, or rather just a quantitative
692 modification of the basic clear-sky picture developed here, provides an interesting avenue for future
693 work.

694 A further important caveat to our work is that the assumption that the midlatitudes provide a
695 boundary condition for the polar RAE regime may be oversimplified. The results of Stuecker et al.
696 (2018) suggest that polar influence is only negligible equatorward of $\sim 45^\circ$ latitude. However, the
697 RAE regime is only holds poleward of around 75° latitude; the $45\text{-}75^\circ$ band contains a mixed

698 radiative-convective-advective equilibrium (RCAE) regime (Miyawaki et al. 2022). However,
699 preliminary experimentation shows some success in predicting the polar warming response of
700 a full-complexity climate model using the single-column model relaxed to the climate model's
701 midlatitude T_e profile. We will report on these results in future work. Nonetheless, better
702 understanding of the physics of the RCAE regime, and its relation the to the tropical RCE and polar
703 RAE regimes, is clearly of considerable interest.

704 *Acknowledgments.* We thank Nadir Jeevanjee, Ming Cai and an anonymous reviewer for their
705 comments.

706 *Data availability statement.* The CliMT modelling framework is available at
707 <https://github.com/CliMT/climt>. The ERA-Interim reanalysis product may be obtained
708 as detailed here: <https://confluence.ecmwf.int/display/CKB/How+to+download+ERA-Interim+data+from+the+ECMWF+data+archive>.
709

710 APPENDIX

711 **Computation of F_{win}**

712 The radiative scheme used in the model provides wavelength-integrated upward and downward
713 fluxes as output, but the numerical implementation makes it difficult to disentangle the surface and
714 atmospheric contributions. Instead, we compute F_{win} indirectly as $F_{\text{win}} = \sigma T_s^4 - F_{\text{abs}}$, where F_{abs}
715 is the part of the surface emission absorbed by the atmospheric column. Using Kirchhoffs's law
716 to note that the surface flux absorbed by an atmospheric layer is equal to the amount that would be
717 received at the surface if that layer emitted at the surface temperature, we estimate F_{abs} through a
718 call to the radiative scheme in which the temperature is set everywhere to its surface value while
719 the humidity and CO₂ distributions are unchanged. This is an approximation because it neglects
720 the temperature dependence of atmospheric emissivity. However, detailed line-by-line calculations
721 show the effect of temperature-dependent opacity on emission is small compared to the direct effect
722 of temperature on the Planck source function (Huang and Ramaswamy 2007; Cronin and Dutta
723 2023), and we assume that the approximation is sufficient for the present purposes, which do not
724 hinge crucially on the exact value of F_{win} .

725 **References**

- 726 Andry, O., R. Bintanja, and W. Hazeleger, 2017: Time-dependent variations in the Arctic's surface
727 albedo feedback and the link to seasonality in sea ice. *J. Climate*, **30**, 393–410.
- 728 Armour, K. C., N. Siler, A. Donohoe, and G. H. Roe, 2019: Meridional atmospheric heat transport
729 constrained by energetics and mediated by large-scale diffusion. *J. Climate*, **32**, 3655–3680,
730 <https://doi.org/10.1175/JCLI-D-18-0563.1>.

- 731 Audette, A., and Coauthors, 2021: Opposite responses of the dry and moist eddy heat transport
732 into the Arctic in the PAMIP experiments. *Geophys. Res. Lett.*, **48**, e2020GL089 990.
- 733 Boeke, R. C., P. C. Taylor, and S. A. Sejas, 2021: On the nature of the Arctic’s positive lapse-rate
734 feedback. *Geophys. Res. Lett.*, **48**, e2020GL091 109.
- 735 Caballero, R., R. Pierrehumbert, and J. Mitchell, 2008: Axisymmetric, nearly inviscid circulations
736 in non-condensing radiative-convective atmospheres. *Quart. J. Roy. Meteor. Soc.*, **134**, 1269–
737 1285.
- 738 Cai, M., 2005: Dynamical amplification of polar warming. *Geophys. Res. Lett.*, **32**, L22 710.
- 739 Cai, M., 2006: Dynamical greenhouse-plus feedback and polar warming amplification. Part I: A
740 dry radiative-transportive climate model. *Clim. Dyn.*, **26**, 661–675.
- 741 Cai, M., and J. Lu, 2007: Dynamical greenhouse-plus feedback and polar warming amplification.
742 Part II: Meridional and vertical asymmetries of the global warming. *Clim. Dyn.*, **29**, 375–391.
- 743 Cai, M., and J. Lu, 2009: A new framework for isolating individual feedback processes in coupled
744 general circulation climate models. Part II: Method demonstrations and comparisons. *Clim.*
745 *Dyn.*, **32**, 887–900.
- 746 Cardinale, C. J., B. E. Rose, A. L. Lang, and A. Donohoe, 2021: Stratospheric and tropospheric
747 flux contributions to the polar cap energy budgets. *J. Climate*, **34**, 4261–4278.
- 748 Chang, C.-Y., and T. M. Merlis, 2023: The role of diffusivity changes on the pattern of warming in
749 energy balance models. *J. Climate*, **36**, 7993–8006.
- 750 Chen, Y.-T., Y. Huang, and T. M. Merlis, 2023: The global patterns of instantaneous CO₂ forcing
751 at the top-of-atmosphere and surface. *J. Climate*, **36**, 6331–6347.
- 752 Chen, Y.-T., T. M. Merlis, and Y. Huang, 2024: The cause of negative CO₂ forcing at the top-
753 of-atmosphere: the role of stratospheric vs. tropospheric temperature inversions. *Geophys. Res.*
754 *Lett.*, **51**, e2023GL106 433.
- 755 Chung, C. E., and P. Räisänen, 2011: Origin of the Arctic warming in climate models. *Geophys.*
756 *Res. Lett.*, **38**, L21 704.

757 Collins, W. D., and Coauthors, 2004: Description of the NCAR community atmosphere model
758 (CAM 3.0). *NCAR Tech. Note NCAR/TN-464+ STR*, **226**.

759 Colman, R., J. Fraser, and L. Rotstayn, 2001: Climate feedbacks in a general circulation model
760 incorporating prognostic clouds. *Clim. Dyn.*, **18**, 103–122.

761 Cronin, T. W., and I. Dutta, 2023: How well do we understand the Planck feedback? *J. Adv. Model.*
762 *Earth Syst.*, **15**, e2023MS003 729.

763 Cronin, T. W., and M. F. Jansen, 2016: Analytic radiative-advective equilibrium as a model for
764 high-latitude climate. *Geophys. Res. Lett.*, **43**, 449–457.

765 Cronin, T. W., and E. Tziperman, 2015: Low clouds suppress Arctic air formation and amplify
766 high-latitude continental winter warming. *Proc. Natl. Acad. Sci. USA*, **112**, 11 490–11 495.

767 Curry, J., 1983: On the formation of continental polar air. *J. Atmos. Sci.*, **40**, 2278–2292.

768 Dimitrellos, A., R. Caballero, and A. M. Ekman, 2023: Controls on surface warming by winter
769 Arctic moist intrusions in idealized large-eddy simulations. *J. Climate*, **36**, 1287–1300.

770 Feldl, N., and T. M. Merlis, 2021: Polar amplification in idealized climates: the role of ice,
771 moisture, and seasons. *Geophys. Res. Lett.*, e2021GL094130.

772 Feldl, N., and T. M. Merlis, 2023: A semi-analytical model for water vapor, temperature,
773 and surface-albedo feedbacks in comprehensive climate models. *Geophys. Res. Lett.*, **50**,
774 e2023GL105 796.

775 Feldl, N., S. Po-Chedley, H. K. Singh, S. Hay, and P. J. Kushner, 2020: Sea ice and atmospheric
776 circulation shape the high-latitude lapse rate feedback. *npj Clim. Atmos. Sci.*, **3**, 1–9.

777 Freese, L. M., and T. W. Cronin, 2021: Antarctic radiative and temperature responses to a doubling
778 of CO₂. *Geophys. Res. Lett.*, **48**, e2021GL093 676.

779 Hahn, L., K. C. Armour, D. S. Battisti, A. Donohoe, A. Pauling, and C. Bitz, 2020: Antarctic
780 elevation drives hemispheric asymmetry in polar lapse-rate climatology and feedback. *Geophys.*
781 *Res. Lett.*, **47**, e2020GL088 965.

782 Hahn, L. C., K. C. Armour, M. D. Zelinka, C. M. Bitz, and A. Donohoe, 2021: Contributions to
783 polar amplification in CMIP5 and CMIP6 models. *Front. Earth Sci.*, **9**, 710 036.

784 Henry, M., T. Merlis, N. Lutsko, and B. E. Rose, 2021: Decomposing the drivers of polar
785 amplification with a single column model. *J. Climate*, **34**, 2355–2365.

786 Henry, M., and T. M. Merlis, 2020: Forcing dependence of atmospheric lapse rate changes
787 dominates residual polar warming in solar radiation management climate scenarios. *Geophys.*
788 *Res. Lett.*, **47**, e2020GL087929.

789 Huang, Y., and V. Ramaswamy, 2007: Effect of the temperature dependence of gas absorption in
790 climate feedback. *J. Geophys. Res. Atmos.*, **112**, D07101.

791 Hwang, Y.-T., D. M. Frierson, and J. E. Kay, 2011: Coupling between Arctic feedbacks and changes
792 in poleward energy transport. *Geophys. Res. Lett.*, **38**, 17704.

793 Jeevanjee, N., and S. Fueglistaler, 2020: Simple spectral models for atmospheric radiative cooling.
794 *J. Atmos. Sci.*, **77**, 479–497.

795 Jeevanjee, N., I. Held, and V. Ramaswamy, 2022: Manabe’s radiative–convective equilibrium.
796 *Bull. Am. Meteorol. Soc.*, **103**, E2559–E2569.

797 Jeevanjee, N., J. T. Seeley, D. Paynter, and S. Fueglistaler, 2021: An analytical model for spatially
798 varying clear-sky CO₂ forcing. *J. Climate*, **34**, 9463–9480.

799 Kim, D., S. M. Kang, T. M. Merlis, and Y. Shin, 2021: Atmospheric circulation sensitivity to
800 changes in the vertical structure of polar warming. *Geophys. Res. Lett.*, **48**, e2021GL094726.

801 Koll, D. D., N. Jeevanjee, and N. J. Lutsko, 2023: An analytic model for the clear-sky longwave
802 feedback. *J. Atmos. Sci.*, doi:10.1175/JAS-D-22-0178.1.

803 Lu, J., and M. Cai, 2009: A new framework for isolating individual feedback processes in coupled
804 general circulation climate models. Part I: Formulation. *Clim. Dyn.*, **32**, 873–885.

805 Lu, J., and M. Cai, 2010: Quantifying contributions to polar warming amplification in an idealized
806 coupled general circulation model. *Clim. Dyn.*, **34**, 669–687.

807 Manabe, S., and R. F. Strickler, 1964: Thermal equilibrium of the atmosphere with a convective
808 adjustment. *J. Atmos. Sci.*, **21**, 361–385.

809 Manabe, S., and R. T. Wetherald, 1967: Thermal Equilibrium of the Atmosphere with a Given
810 Distribution of Relative Humidity. *J. Atmos. Sci.*, **24**, 241–259.

- 811 Manabe, S., and R. T. Wetherald, 1980: On the distribution of climate change resulting from an
812 increase in the CO₂ content of the atmosphere. *J. Atmos. Sci.*, **37**, 99–118.
- 813 Merlis, T. M., and M. Henry, 2018: Simple estimates of polar amplification in moist diffusive
814 energy balance models. *J. Climate*, **31**, 5811–5824.
- 815 Miyawaki, O., T. A. Shaw, and M. F. Jansen, 2022: Quantifying energy balance regimes in the
816 modern climate, their link to lapse rate regimes, and their response to warming. *J. Climate*, **35**,
817 1045–1061.
- 818 Miyawaki, O., T. A. Shaw, and M. F. Jansen, 2023: The emergence of a new wintertime Arctic
819 energy balance regime. *Environ. Res.: Climate*, **2**, 031 003.
- 820 Monteiro, J. M., and R. Caballero, 2016: The Climate Modelling Toolkit. *Proceedings of the 15th*
821 *Python in Science Conference (SciPy 2016)*, 69 – 74, doi:10.25 080/Majora-629e541a-014.
- 822 Monteiro, J. M., J. McGibbon, and R. Caballero, 2018: sympl (v. 0.4. 0) and climt (v. 0.15.
823 3)–towards a flexible framework for building model hierarchies in Python. *Geosci. Model Dev.*,
824 **11**, 3781–3794.
- 825 Overland, J. E., and P. Turet, 1994: Variability of the atmospheric energy flux across 70°N
826 computed from the GFDL Data Set. *The Polar Oceans and Their Role in Shaping the Global*
827 *Environment*, Geophys. Monogr., Vol. 85, American Geophysical Union, 313–325.
- 828 Papritz, L., S. Murto, M. Röthlisberger, R. Caballero, G. Messori, G. Svensson, and H. Wernli,
829 2023: The role of local and remote processes for wintertime surface energy budget extremes
830 over Arctic sea ice. *J. Climate*, **36**, 7657–7674.
- 831 Park, K., S. M. Kang, D. Kim, M. F. Stuecker, and F.-F. Jin, 2018: Contrasting local and remote
832 impacts of surface heating on polar warming and amplification. *J. Climate*, **31**, 3155–3166.
- 833 Pauluis, O., A. Czaja, and R. Korty, 2010: The global atmospheric circulation in moist isentropic
834 coordinates. *J. Climate*, **23**, 3077–3093.
- 835 Payne, A. E., M. F. Jansen, and T. W. Cronin, 2015: Conceptual model analysis of the influence of
836 temperature feedbacks on polar amplification. *Geophys. Res. Lett.*, **42**, 9561–9570.

837 Pierrehumbert, R. T., 1995: Thermostats, radiator fins and the local runaway greenhouse. *J. Atmos.*
838 *Sci.*, **52**, 1784–1806.

839 Pithan, F., and T. Jung, 2021: Arctic amplification of precipitation changes—the energy hypothesis.
840 *Geophys. Res. Lett.*, **48**, e2021GL094977.

841 Pithan, F., and T. Mauritsen, 2014: Arctic amplification dominated by temperature feedbacks in
842 contemporary climate models. *Nat. Geosci.*, **7**, 181–184.

843 Pithan, F., and Coauthors, 2018: Role of air-mass transformations in exchange between the Arctic
844 and mid-latitudes. *Nat. Geosci.*, doi:10.1038/s41561-018-0234-1.

845 Previdi, M., K. L. Smith, and L. M. Polvani, 2021: Arctic amplification of climate change: a
846 review of underlying mechanisms. *Environ. Res. Lett.*, **16**, 093003.

847 Salzmann, M., 2017: The polar amplification asymmetry: role of Antarctic surface height. *Earth*
848 *Syst. Dynam.*, **8**, 323–336.

849 Screen, J. A., C. Deser, and I. Simmonds, 2012: Local and remote controls on observed arctic
850 warming. *Geophysical Research Letters*, **39**, L10709.

851 Seeley, J. T., and N. Jeevanjee, 2021: H₂O windows and CO₂ radiator fins: A clear-sky explanation
852 for the peak in equilibrium climate sensitivity. *Geophys. Res. Lett.*, **48**, e2020GL089609.

853 Semmler, T., F. Pithan, and T. Jung, 2020: Quantifying two-way influences between the Arctic and
854 mid-latitudes through regionally increased CO₂ concentrations in coupled climate simulations.
855 *Clim. Dyn.*, **54**, 3307–3321.

856 Shaw, T. A., and Z. Tan, 2018: Testing latitudinally dependent explanations of the circulation
857 response to increased CO₂ using aquaplanet models. *Geophys. Res. Lett.*, **45**, 9861–9869.

858 Sherwood, S. C., S. Bony, O. Boucher, C. Bretherton, P. M. Forster, J. M. Gregory, and B. Stevens,
859 2015: Adjustments in the forcing-feedback framework for understanding climate change. *Bull.*
860 *Am. Meteorol. Soc.*, **96**, 217–228.

861 Soden, B. J., I. M. Held, R. Colman, K. M. Shell, J. T. Kiehl, and C. A. Shields, 2008: Quantifying
862 climate feedbacks using radiative kernels. *J. Climate*, **21**, 3504–3520.

- 863 Stuecker, M. F., and Coauthors, 2018: Polar amplification dominated by local forcing and feed-
864 backs. *Nat. Clim. Change*, **8**, 1076–1081.
- 865 Taylor, P. C., and Coauthors, 2022: Process drivers, inter-model spread, and the path forward: A
866 review of amplified Arctic warming. *Front. Earth Sci.*, **9**, 758 361, [https://doi.org/10.3389/feart.](https://doi.org/10.3389/feart.2021.758361)
867 2021.758361.
- 868 Trenberth, K. E., 1991: Climate diagnostics from global analyses: Conservation of mass in
869 ECMWF analyses. *J. Climate*, **4**, 707–722.
- 870 Wexler, H., 1936: Cooling in the lower atmosphere and the structure of polar continental air. *Mon.*
871 *Wea. Rev.*, **64**, 122–136.
- 872 Woods, C., and R. Caballero, 2016: The role of moist intrusions in winter Arctic warming and sea
873 ice decline. *J. Climate*, **29**, 4473–4485.
- 874 Yoshimori, M., A. Abe-Ouchi, and A. Laîné, 2017: The role of atmospheric heat transport and
875 regional feedbacks in the arctic warming at equilibrium. *Clim. Dyn.*, **49**, 3457–3472.